Wave propagation and focusing of soft X-rays by spherical bent microchannel plates

M. I. Mazuritskiy,[a]* A. M. Lerer,[a] A. Marcelli,[b,c,d] S. B. Dabagov,[b,e,f] M. Coreno,[d] A. D'Elia[g] and S. J. Rezvani[b,g]

[a]Physics Department, Southern Federal University, 344090 Rostov-on-Don, Russian Federation, [b]INFN – Laboratori Nazionali di Frascati, via Enrico Fermi 54, 00044 Frascati, Italy, [c]RICMASS – Rome International Center for Materials Science Superstripes, 00185 Rome, Italy, [d]Istituto Struttura della Materia, CNR, Via del Fosso del Cavaliere 100, 00133 Rome, Italy, [e]RAS P. N. Lebedev Physical Institute, 119991 Moscow, Russian Federation, [f]NR Nuclear University MEPhI, 115409 Moscow, Russian Federation, and [g]IOM-CNR, Laboratorio Nazionale TASC, Basovizza SS-14, km 163.5, 34012 Trieste, Italy. *Correspondence e-mail: mazurmik@gmail.com

Synchrotron radiation sources have been used to study the focusing properties and angular distribution of X-ray radiation at the exit of spherically bent microchannel plates (MCPs). In this contribution it is shown how soft X-ray radiation at energies up to 1.5 keV can be focused by spherically bent MCPs with curvature radii R of 30 mm and 50 mm. For these devices, a focus spot is detectable at a distance between the detector and the MCP of less than $R/2$, with a maximum focusing efficiency up to 23% of the flux illuminating the MCP. The soft X-ray radiation collected at the exit of microchannels of spherically bent MCPs are analyzed in the framework of a wave approximation. A theoretical model for the wave propagation of radiation through MCPs has been successfully introduced to explain the experimental results. Experimental data and simulations of propagating radiation represent a clear confirmation of the wave channeling phenomenon for the radiation in spherically bent MCPs.

1. Introduction

Nowadays synchrotron radiation (SR) sources and X-ray free-electron lasers (XFELs) provide powerful and brilliant X-ray beams that allow the structure and dynamics of matter to be investigated from atomic to mesoscale distances (Tsuji *et al.*, 2004). Actually, brilliant X-ray spots are becoming more and more important for studying complex and functional materials at low dimensions or complex phenomena such as strain-driven metal–insulator transition strongly correlated systems (D'Elia *et al.* 2020), structural confinement in semiconducting nanowires (Rezvani *et al.*, 2016; Pinto *et al.*, 2016) and electrochemical dynamics of metal oxide nanoparticles (Rezvani *et al.*, 2018; Pasqualini *et al.*, 2017). Hence, generating a brilliant spot size is a challenging issue, but extremely important for a large class of experiments. Moreover, the continuously growing demand for low-emittance SR sources and XFELs requires new optical elements capable of focusing or shaping radiation as well as filtering or shifting the energy of the X-ray beam (Cao *et al.*, 2013).

Many applications of X-ray focusing optics made by hollow glass microchannels working with both X-ray tubes and synchrotron radiation sources exist (Kumakhov, 2000; Gao & Janssens, 2004). They are mainly associated with small beam size and with the increase of the flux density (MacDonald & Gibson, 2000; Gao & Janssens, 2004; Dabagov & Gladkikh, 2019).

Properties and characteristics of X-ray radiation at the exit of a polycapillary device have been investigated since the
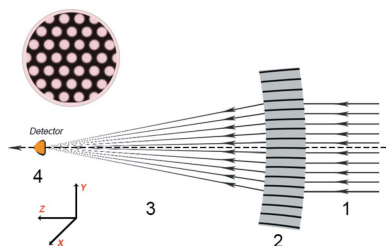
1990s (Kumakhov *et al.*, 1990; Bilderback *et al.*, 1994; Dabagov *et al.*, 1995a; Dabagov, 2003a, MacDonald, 2010). Some devices have been used in applications requesting both high flux density and small spot size, *i.e.* in the micrometre and sub-micrometre ranges (Pfeiffer *et al.*, 2002; Dabagov, 2003b; Bukreeva *et al.*, 2010; Sun *et al.*, 2009; Dabagov & Gladkikh, 2019). Since then, arrays of curved and tapered capillaries have been used to focus, collimate and filter X-ray radiation (Gao & Janssens, 2004). Moreover, for the next generation of coherent UV and X-ray sources, new optics and dedicated experimental devices are required so that the propagation control of soft X-ray radiation through compact focusing devices is an extremely important issue.

Among various X-ray optical elements, the compact and flexible microchannel plate (MCP) devices are versatile and low-cost systems suitable for condensing and shaping intense X-ray beams. MCPs are relatively thin silicon–lead glass samples where identical holes, with shapes from circular to triangular, are drilled. MCPs made with circular holes are usually characterized by a length-to-diameter ratio of about 100. These devices typically contain thousands to millions of miniature hole microchannels oriented parallel to each other and regularly distributed with both pattern and symmetry well defined. In our case the symmetry in the transverse cross-section is hexagonal (Gys, 2015; Mazuritskiy *et al.*, 2019). Similar to polycapillary lenses (Kumakhov & Komarov, 1990), MCP devices offer numerous advantages, for instance, the possibility to enhance both the radiation density and the image resolution at soft X-ray energy (Gao & Janssens, 2004; Brunton *et al.*, 1999).

MCPs have been used in small-angle scattering probes, powder diffractometers, micro-fluorescence spectrometers, *etc.* (Gao & Janssens, 2004). They can also be applied as a condenser in a soft X-ray microscope coupled to a plasma X-ray source (Cao *et al.*, 2013). Furthermore, studies on the propagation of X-ray radiation inside MCPs are particularly interesting for improving the spot stability and for optimizing the characteristics of a soft X-ray beam, *e.g.* in the 'water window' region. Previous studies (Zhang *et al.*, 2014; Zhurong *et al.*, 2013) have also used MCPs to tune the energy as well as the bandwidth of the beam. By changing the incidence angle of the radiation and the length-to-width ratio of the channels, MCPs can also be used to filter the transmitted radiation (Cao *et al.*, 2013). Finally, experimental and theoretical efforts are in progress to exploit the use of MCPs for fluorescence applications (Mazuritskiy, 2012; Mazuritskiy *et al.*, 2014) and as diffractive devices (Mazuritskiy *et al.*, 2016a,b, 2018) in combination with different layouts and X-ray sources.

X-rays focusing by MCPs has been studied since the 1990s (Chapman *et al.*, 1990, 1993; Kaaret *et al.*, 1992; Nussey, 2005). In these early studies the analysis of radiation propagation through MCPs was based on X-ray multiple reflections from the internal walls of microchannels. This approach, however, does not consider the phase evolution of propagating waves and, thus, the possible interference among different components of the radiation (Dabagov *et al.*, 1995b). We should emphasize here that the description of the X-ray transmission of any geometrical configuration used to bend, focus and collimate radiation has to consider the wave theory of X-ray propagation. The latter may allow describing the radiation distribution patterns behind MCPs. Indeed, the radiation propagation inside microchannels is dominated by the radiation interaction with the inner channel surface, and also the propagation of surface waves along the channel walls cannot be neglected (Dabagov, 2003a). In this work, we present and discuss original experimental data as well as simulations of the spatial distribution of soft X-ray radiation after spherically bent MCPs having different curvature radii.

2. Experimental setup

We have measured angular distributions of X-ray radiation emerging from spherical bent MCPs composed of many cylindrical channels. Flat MCPs are formed by arrays of 10^4–10^7 hollow microchannels, regularly separated, and arranged within a defined symmetry. In our case, we characterized devices with hexagonal symmetry in the transverse cross-section and channels oriented parallel to each other [see Fig. 1(a)].

MCP devices manufactured by BASPIK (Vladikavkaz, Russia) are made by silicon–lead glasses with a mass-concentration (SiO_2:PbO) ratio of about 1:2. Channel axes are normal to the surface and their inner surfaces are characterized by a low roughness (<5 nm). The standard thickness of these MCPs is in the range 0.2–0.8 mm, but we investigated also plates up to ∼1.3–1.5 mm thick. In the transverse cross-section, the hexagonal pattern is made by long channels with a diameter of 10 µm and a pitch size of 12 µm. The open area fraction of flat MCPs is about 60%.

Spherically bent MCPs [Fig. 1(b)] were manufactured by applying to a flat device a special technology developed at the Southern Federal University together with BASPIK. The spherical shape was achieved by the combined application of pressure and temperature, *i.e.* via the inelastic deformation of
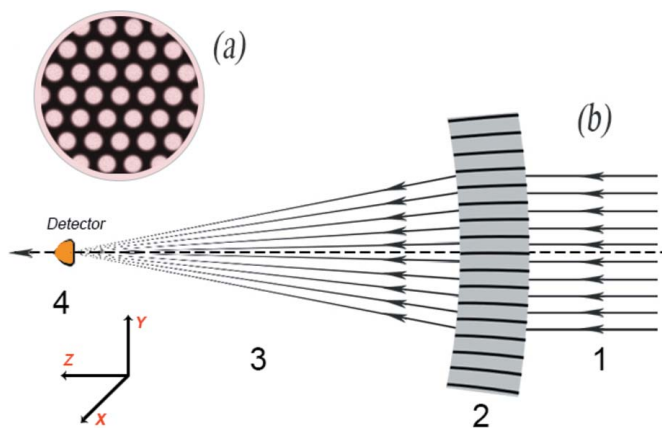

Figure 1
Experimental layout of the focusing geometry of a spherical MCP: (a) the channels pattern; (b) 1 – primary beam, 2 – spherically bent MCP, 3 – propagating radiation, 4 – detector.

the original flat device using stainless mandrels with radii of 30 mm and 50 mm.

In Fig. 1(*b*) the MCP spherical surface is illuminated from the right-hand side by a monochromatic radiation beam with divergence <5 mrad. X-rays propagate inside MCP micro-channels and are collected at the exit by the detector. The latter can be set at different transversal (xy) positions and different distances along the z-axis.

Transmission measurements were performed for different energies of the primary radiation transmitted by two MCPs of different curvature radii. The angular distributions of the radiation after the MCP with diameter 33 mm and thickness 1.3 mm were measured both at the BESSY II SR facility and at the ELETTRA SR laboratory at the CiPo beamline of the Elettra SR facility at Trieste (https://www.elettra. trieste.it/it/lightsources/elettra/elettra-beamlines/cipo/cipo beamline.html).

At BESSY II the MCP was installed in the vacuum chamber of the Reflectometer end-station, available at the XUV-Optics beamline. This apparatus has five goniometric circles: three for the sample scan and two for the detector alignment. The UHV-Reflectometer layout is described in dedicated papers (Sokolov *et al.*, 2014, 2018). The beam divergence at the sample position is 0.5 mrad × 3.6 mrad (V × H). This station enables the effective vertical size of the X-ray monochromatic primary radiation illuminating the MCP device to be fixed within the range 0.1–1.0 mm. Setting the vertical parameter at 0.5 mm we measured the distribution of the X-ray radiation intensity at the MCP exit, *i.e.* the total photon flux density, and the focusing properties in the range 1000–1500 eV at different distances between the device and the detector along the z-axis [Fig. 1(*b*)]. The focused radiation has been collected at different distances behind the spherically bent MCP measuring at each position the radiation spot dimension. This analysis allowed obtaining the minimal spot size with the highest collected radiation density.

At BESSY, to measure the radiation intensity we used a gold plate as detector. The total electrical current generated by the radiation on the surface of the metal gold plate was calibrated to obtain the integrated intensity. The accurate rotation of the detector around the vertical direction on the 'xy'-plane (at the exit of the MCP) allowed measuring the total intensity at different 'z-distances'. A map was obtained by measuring the intensity at different distances between the MCP and the detector.

Similar studies have been performed at the Circularly Polarization (CiPo) beamline at Elettra (Trieste) using a high-vacuum experimental chamber (Marcelli *et al.*, 2004) and the setup shown in Fig. 2 (Marcelli *et al.*, 2018).

To observe the radiation distribution after the optical device under test, an elliptically shaped fluorescent YAG screen (diameter D = 25 mm) has been installed about 130 cm downstream from the optics. Under X-ray irradiation, the YAG screen, acting as a scintillator, emits visible light trans-forming the X-ray distribution into a pattern at visible wave-lengths. The YAG screen was inclined at 45° with respect to the incident light propagation and at 45° also with respect
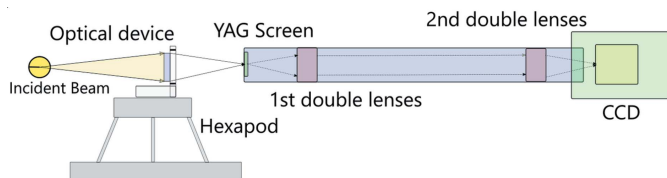

Figure 2
Experimental setup available at CiPo (Elettra) with the YAG screen used to observe the X-ray spot generated by the spherically bent MCP.

to the CCD detector (Basler model scA640-120gm/gc). The resolution of the 2D detector is 1 pixel = 13 ± 1.3 μm; it has been measured by placing a 100 μm-wide filament and measuring the signal.

A high-precision manipulator that consists of a hexapod system characterized by six degrees of freedom and large travel ranges was used to align the MCP. The motion ranges of the hexapod are: ±25 mm (x, z), ±6.25 mm (y) and ±5° (θx, θy, θz). This sample-positioning system offers bidirectional repeatability of ±0.5 μm (x, y, z) and ±20 μrad (θx, θy, θz) working at the minimum operating pressure of 10^{-7} mbar. With this layout, we recorded the angular distribution of the radiation after the spherical MCP at the photon energy of 450 eV using the 2D CCD detector installed inside the HV chamber. A pinhole of diameter D = 300 μm was set in front of the MCP to preserve the spatial coherence property of the primary beam generated by the undulator. In this layout, hence, the aperture of the primary radiation at the MCP entrance is defined by the pinhole.

3. Results and discussion

To characterize the focusing properties of an optical element a precise characterization of the spatial distribution of the transmitted radiation is mandatory. 2D maps of transmitted radiation behind MCPs are shown in Figs. 3 and 4 as functions of the position of the CCD detector (xy plane) and along the z-axis (perpendicular to the CCD plane), respectively. The energy of the primary SR radiation for both figures is 450 eV.

Fig. 3 demonstrates the change of both shape and topology for transmitted radiation distribution with respect to the MCP position in the xy plane, *i.e.* the detector plane. Maps clearly show that the line connecting the center of the spherical MCP surface with the geometrical focus should be aligned with the primary radiation direction to obtain the focal spot. Any misalignment generates circular or donut-shaped distribu-tions. Once the beam and MCP are properly aligned, the spot size reduction as a function of the MCP–CCD distance is clearly visible, as shown in Fig. 4. The line profile of the central spot can be fitted with a Gaussian profile, whose parameters are used to characterize the focusing properties, as discussed below.

The maps shown in Figs. 3 and 4 correspond to data collected at the Elettra CiPo beamline at the energy of 450 eV, while experiments at BESSY were previously performed at higher photon energies, *i.e.* 1000 eV and 1500 eV.
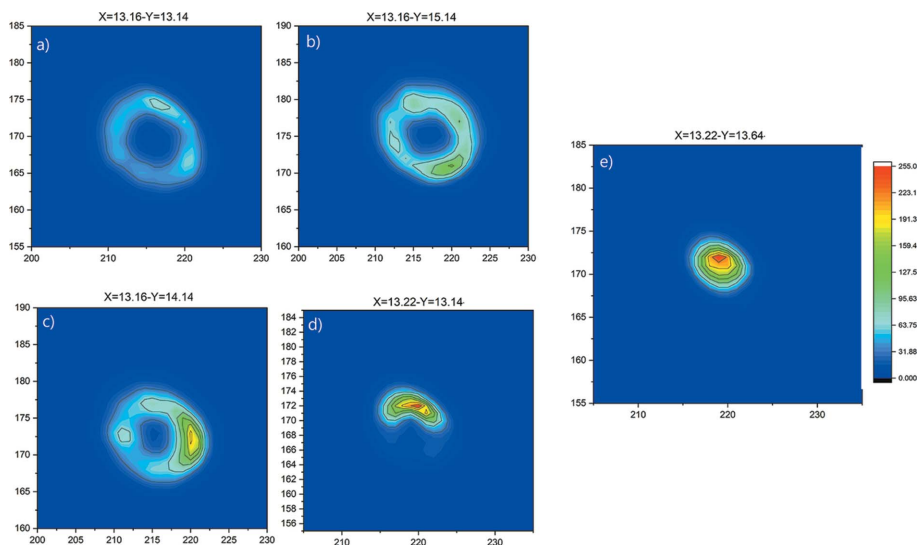
Figure 3
Radiation distribution patterns of the MCP with bending radius $R = 30$ mm at $z = 15$ mm. The color bar refers to the radiation intensity. Maps have been collected moving the MCP in the x direction from ~ 13 to ~ 14 mm and in the y direction from ~ 13 to ~ 15 mm. The xy coordinates of each map are shown at the top. The area in each panel is constant (30×30 pixels) and the numbers on the xy-axis are pixels.
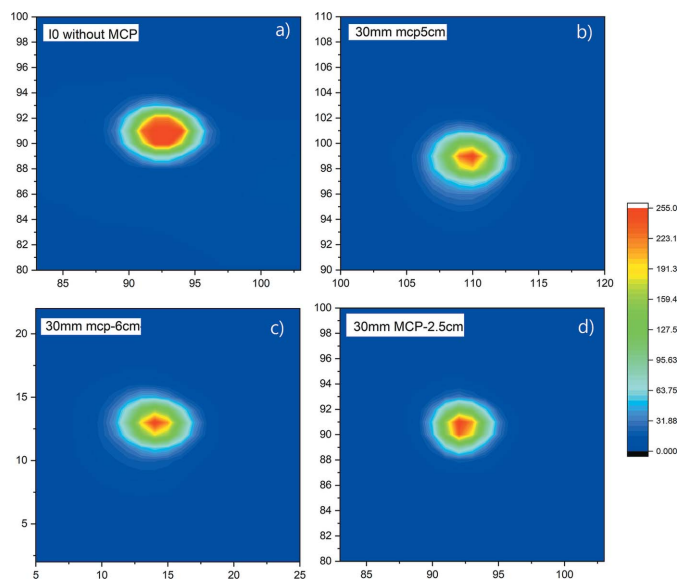

Figure 4
Maps obtained translating the MCP along the z-axis (*i.e.* changing the distance between the MCP and the CCD). The color bar refers to the radiation intensity. The area in each panel is constant (20×20 pixels) and the xy-axes are expressed in pixels. The map of the incident beam is top left while other maps correspond to distances of 25, 50 and 60 mm along the z-axis.

Figs. 5(a)–5(c) show line profiles (in the xz plane) of the 2D spatial distributions for MCPs with the curvature radius of 30 and 50 mm at different energies ($E = 450$ eV at Elettra, $E = 1000$ eV and 1500 eV at BESSY) for different distances along the z-axis. Fig. 5(d) shows a 2D presentation of the radiation distribution at the energy of 450 eV.

As shown in Figs. 5(a) and 6(a), using a Gaussian profile, the fit points out the decrease of the full width half-maximum (FWHM). The smallest dimension of the spot and the maximum intensity is achieved at $z = 15$ mm, which unfortunately was the shortest possible distance we were able to reach with the MCP with radius 30 mm at 450 eV energy. At this distance the FWHM of the profile in the xz plane is 39 μm and, in this position, the intensity referred to the primary beam intensity is 18%. The result demonstrates that a spherically bent MCP focuses the incident radiation, and the smallest spot is achieved by a careful alignment of the bent MCP with respect to the primary radiation direction. The variation of the spot size as a function of the MCP–detector distance at three different energies is shown in Fig. 6.

The evolution of the 2D line profiles as well as the FWHM for the MCP with a curvature radius of 50 mm reveals that the profile of the spot is narrower at the distance $z = 18$ mm between the spherically bent MCP and the detector at 1000 eV. At this distance, the FWHM is 43 μm and, in this position, the intensity referred to the intensity of the primary beam is $\sim 20\%$. At the energy of 1500 eV the spot is smaller at the distance of 20 mm, the FWHM is ~ 57 μm and the corresponding intensity in this position is $\sim 23\%$ of the primary beam intensity.

Experimental data in Fig. 6 for different spherically bent MCPs ($R = 30$ mm and $R = 50$ mm) show also a functional dependence of the spot size versus the distance. This study clearly shows that the most brilliant spots recorded after spherically bent MCPs occurs at distances $< R/2$.

The result is not in agreement with data published in the 1990s (Chapman *et al.*, 1990, 1993; Kaaret *et al.*, 1992; Nussey, 2005) where the focus was set at about half of the curvature radius. In those manuscripts, the authors discussed the results using a geometrical optical method, analogous to the propagation of visible radiation through a thin lens. Within this approximation, valid only at no thickness or for extremely thin MCP plates, the focus has to occur along the optical axis at a distance equal to half of the curvature radius.

Our result obtained for rather thick MCP plates can be explained considering the redistribution of the primary radiation hitting the MCP surface and the propagation along inclined (and bent) channels. Bending flat MCPs, the originally cylindrical channels are conically deformed and, as a consequence, a more efficient reflection process occurs due to the higher angle of grazing, along with radiation channeling. This mechanism determines a focal distance closer to the MCP and then focus is achieved at distances $< R/2$.
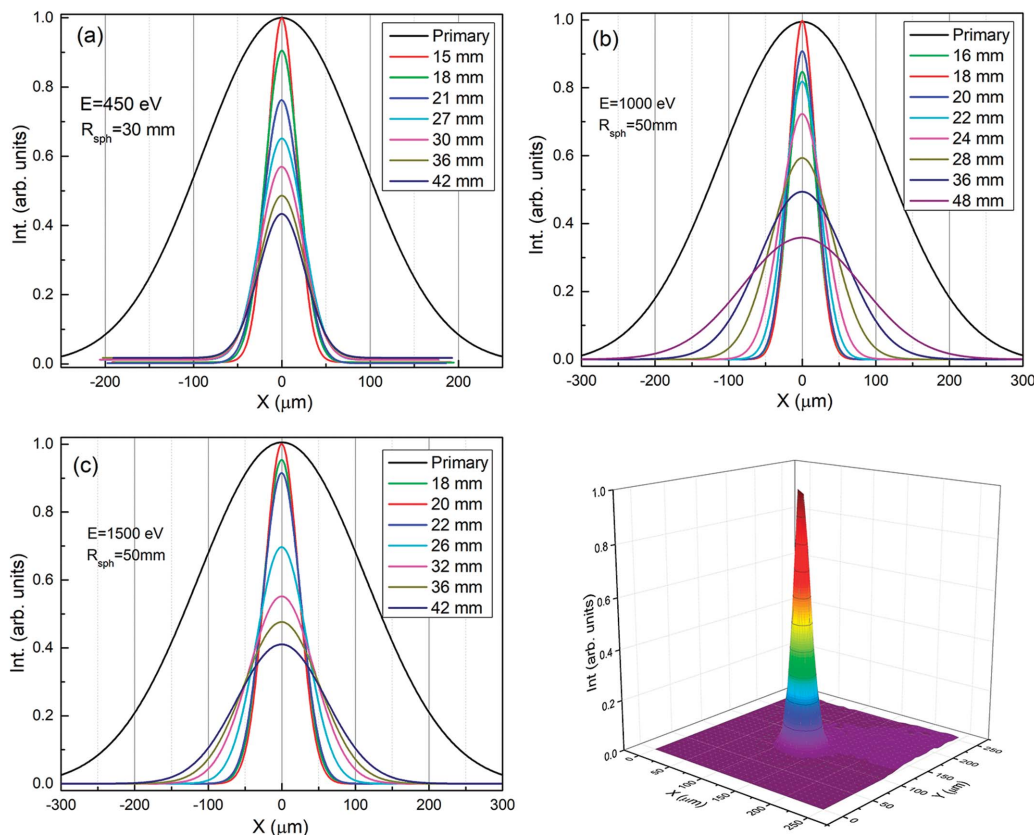
Figure 5
Comparison of profiles and spot sizes (FWHM) of radiation collected by MCPs with two different radii of curvature at different energies: (a) 450 eV Elettra, (b) 1000 eV BESSY and (c) 1500 eV BESSY. All profiles have been normalized to the incident photon flux. Panel (d) shows a 3D profile of focused radiation at 450 eV.

In the geometrical optical approximation no wave-like contributions have to be considered for a fully incoherent source like a conventional source or wide-aperture bending magnet source at a synchrotron radiation facility. For incoherent radiation the geometrical optics approximation is valid. In our case we have applied the wave model, which assumes a fully coherent soft X-ray source (like for third-generation synchrotron radiation sources).

In addition, to explain the experimental data and, in particular, the observed spatial distributions we need to introduce a mathematical model based on the wave propagation (or radiation channeling). Moreover, we have to take into account the interference phenomena of radiation emerging from the exit of spherical MCPs, and for modeling the wave propagation we need to use amplitudes and phases with both real and imaginary parts of the permittivity. Here, we describe MCP devices as multi-capillary systems consisting of hollow cylindrical waveguides made by a silicate glass. We can expect that in bent MCPs the microchannel shapes are changed from cylindrical to conical. In our calculations we did
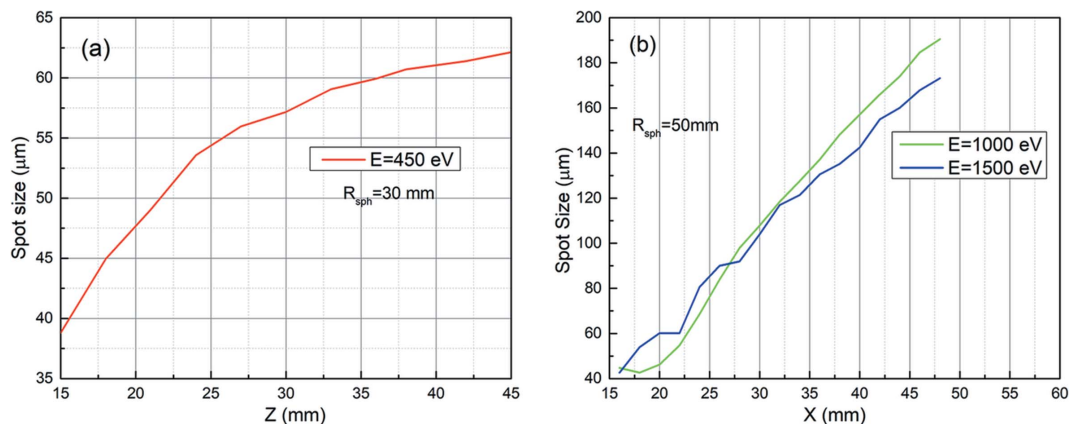

Figure 6
Spot size versus distance between sample and detector for two different spherical bent MCPs.

not use microchannels with a conical shape because for spherical radii of 30–50 mm and MCP thickness of ∼1 mm the changes in the waveguide structure are negligible.

In this model, a flat MCP with a hexagonal lattice is described by the coordinates of the channel centers: $y_q = qd_y$, $x_{pq} = y_q \tan \zeta + pd_x$, where d_x, d_y are the parameters of the lattice and $\zeta = \pi/6$, $-P \leq p \leq P$, $-Q \leq q \leq Q$. The P, Q parameters were determined looking at the dimension of the illuminated area of the MCP and at the dimension of the incident X-ray beam.

The center of the spherical MCP is set at the origin of the coordinate system ($z = 0$) with the axis of this spherical surface lying along the z-axis. The axes of the microchannels are perpendicular to the surface and have directions along the radii of the spherical surface. As a consequence, changing the radius of curvature, moving out from the z-axes, the axes of the microchannels are no longer parallel.

We assume now an unpolarized plane wave $U^{\text{ext}} = \exp(-ikz)$ hitting the curved surface of the MCP and coordinates x_{pq}, y_q of the spherically bent MCP identical to those of the flat plate. This assumption is valid only for small dimensions of the primary beam profile. Using the value of x_{pq}, y_q we can find the coordinates of z_{pq} and the angles θ_{pq}^{ext} [$\sin(\theta_{pq}^{\text{ext}}) = (x_{pq}^2 + y_{pq}^2)^{1/2}/R$] between the axes of the microchannels and the primary beam direction.

The excitation and the propagation of the radiation inside microchannels is described using the Kirchhoff method. In general, we took into account 'N' waveguide modes, which can be excited in each channel. We assume also that the field in the channel has cylindrical symmetry and, neglecting the field outside the microchannel walls (assuming that all radiation is trapped inside channels), we can write the equation for the radiation propagation along the waveguide center,

$$U_{pq}(z') = \sum_{n=1}^{N} \frac{1}{I(\kappa_n, \kappa_n)} I\left[\kappa_n, k \sin(\theta_{pq}^{\text{ext}})\right] \exp(-i\gamma_n z'),$$

where k is the wavenumber, γ_n is the propagation constant of the nth mode for $\kappa_n = (k^2 - \gamma_n^2)^{1/2}$, and z' is the axis of the channel. $I(\kappa, \eta)$ can be defined as the following combination of Bessel functions,

$$I(\kappa, \eta) =$$
$$\begin{cases} a\left[\kappa J_1(\kappa a) J_0(\eta a) - \eta J_0(\kappa a) J_1(\eta a)\right]/(k^2 - \eta^2), & \kappa^2 \neq \eta^2, \\ (a^2/2)\left\{[J_0(\eta a)]^2 + [J_1(\eta a)]^2\right\}, & \kappa^2 = \eta^2. \end{cases}$$

Here a is the radius of the microchannel, J_0, J_1 are Bessel functions and the parameter κ has one of the κ_n values. We consider waves propagating through hollow waveguides of length 'h' with different modes (identified by 'n') towards the exit of the microchannel so that the radiation field outside is defined by the following expressions,

$$U(\theta_{pq}^{\text{ext}}, r_{pq}, \theta_{pq}) = \frac{\exp(-ikr_{pq})}{2\pi r_{pq}} \Phi(\theta_{pq}^{\text{ext}}, \theta_{pq}), \qquad (1)$$

$$\Phi(\theta_{pq}^{\text{ext}}, \theta_{pq}) = \sum_{n=1}^{N} \frac{1}{I(\kappa_n, \kappa_n)} I\left[\kappa_n, k \sin(\theta_{pq}^{\text{ext}})\right]$$
$$\times I\left[\kappa_n, k \sin(\theta_{pq})\right] \exp(-i\gamma_n h), \qquad (2)$$

where r_{pq} is the distance from the exit of the microchannel center to the observation point and θ_{pq} is the angle between the vector $\mathbf{r}_{pq}$ and the channel axis. All parameters are determined using the coordinates (x, y, z) of the observation point,

$$r_{pq} = \left(\bar{x}_{pq}^2 + \bar{y}_{pq}^2 + \bar{z}_{pq}^2\right)^{1/2}, \qquad \theta_{pq} = \alpha_1 - \alpha_2,$$

where $\bar{x}_{pq} = x - x_{pq}$, $\bar{y}_{pq} = y - y_{pq}$, $\bar{z}_{pq} = z - z_{pq}$, $\sin \alpha_1 = 1 - z_{pq}/R$, $\sin \alpha_2 = z - z_{pq}/r_{pq}$.

At X-ray energies and considering the channel radii we deal with a large number of excited waveguide modes that allow the summation in equation (2) to be replaced by the integration over the angular range from $-\vartheta_c$ to ϑ_c,

$$\Phi(\theta_{pq}^{\text{ext}}, \theta_{pq}) = \int_{-\vartheta_c}^{\vartheta_c} \frac{1}{I(\kappa, \kappa)} I\left[\kappa, k \sin(\theta_{pq}^{\text{ext}})\right]$$
$$\times I\left[\kappa, k \sin(\theta_{pq})\right] \exp(-i\gamma h) \, d\kappa, \qquad (3)$$

where $\vartheta_c = k \sin \theta_c$ is the critical angle of the total X-ray reflection. The integral in equation (3) can be solved numerically.

The space distribution of the intensity can be determined using the $\Phi(\theta_{pq}^{\text{ext}}, \theta_{pq})$ function. In the spherical coordinate system the maximum values of $\Phi(\theta_{pq}^{\text{ext}}, \theta_{pq})$ correspond to $\theta_{pq} = \pm\theta_{pq}^{\text{ext}}$. If radiation hits the walls of a hollow cylindrical waveguide at a certain angle, the maximum intensity of the radiation at the output occurs at the same angle, in any direction around the microchannel axis. In other words, at the exit of a single waveguide, we may observe a conical spatial distribution. In the simulation and data presented in Figs. 7(a), 7(c) and 8 we considered the intensity as the Poynting vector of the radiation.

In Fig. 7(a) we show the profile of the propagation at the exit of microchannels with a narrow intensity distribution near θ_{pq}^{ext}. The widths of these maxima decrease increasing both the energy and the diameter of the microchannel waveguide. At a long distance (far-zone) from the exit of the microchannels illuminated by the radiation, the field U_s of the radiation traveling through a MCP can be written as

$$U_s(x, y, z) = \sum_{p=-P}^{P} \sum_{q=-Q}^{Q} U(\theta_{pq}^{\text{ext}}, r_{pq}, \theta_{pq}). \qquad (4)$$

As expected, Fig. 7(b) shows the reflection at different angles of the primary radiation revealing, for radiation propagating inside channels, the decrease of the X-ray reflection at large angles. This dependence should be taken into account in the framework of the above-mentioned model.

To calculate the radiation intensity in the focal spot our model takes into account both amplitudes and phases of X-ray waves at the exit of the microchannels. For these silicate glass waveguides, we used the real and the imaginary parts of the
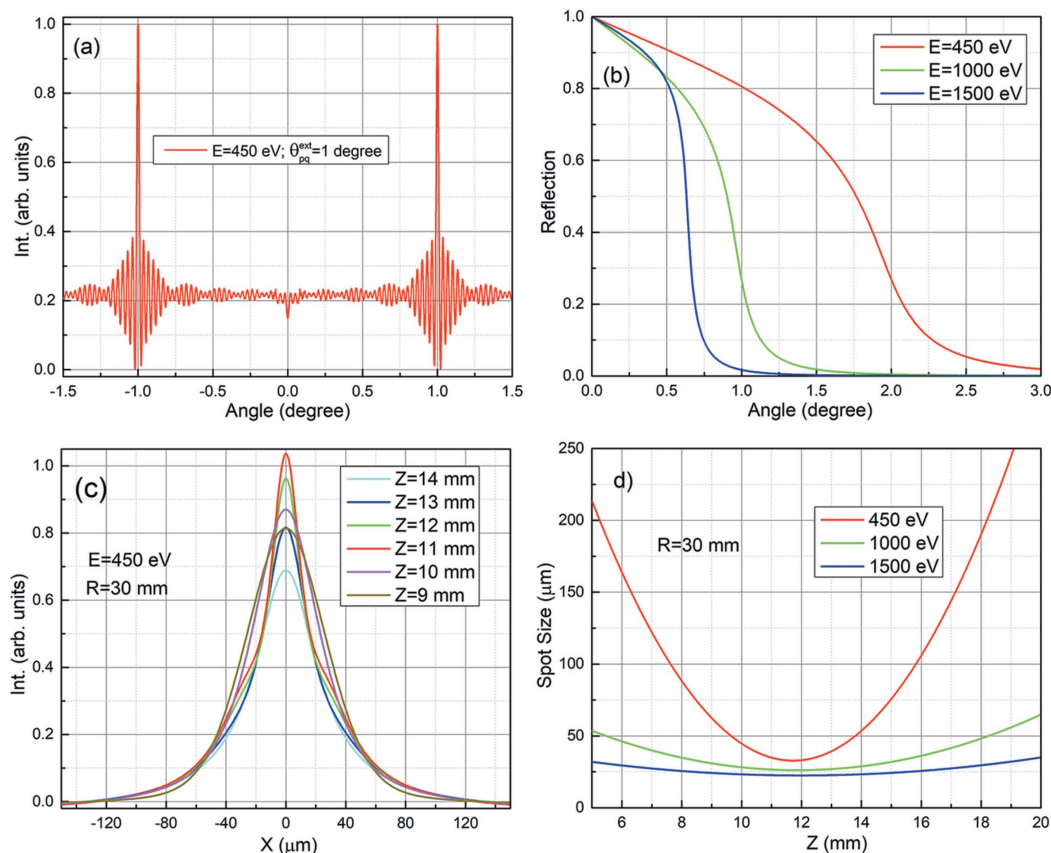
Figure 7
Theoretical simulations: (*a*) the angular distribution of the radiation at the exit of a single waveguide at $E = 450$ eV and $\theta_{pq}^{ext} = 1°$; (*b*) the reflected radiation as a function of the incidence angle at different energies; (*c*) spot profile at different distances between the MCP and the detector; (*d*) the focal spot size versus distance between the MCP ($R = 30$ mm) and the detector at different energies.

refractive index values (Henke *et al.*, 1993). The channels of the MCPs used in this study have a roughness of <5 nm. We had no possibility of confirming this parameter with independent measurements and the mathematical model does not consider the roughness. Actually, this parameter should affect the efficiency of the device, although roughness may substantially introduce a diffused background at the exit. Already in the 1990s one of us considered the contribution of roughness versus slope error in optics (Sanchez del Rio & Marcelli, 1992). We will consider the roughness in an improved mathematical model.

The most intense output was achieved at angles equal to the incident angle of the primary monochromatic radiation. Actually, in previous works on flat MCPs (Mazuritskiy *et al.*, 2014, 2016*a,b*) we have found the same conical space distribution. This pattern will take place from microchannels located at different distances from the center of the spherically bent MCP. However, with respect to the *z*-axis the angles at which intensity maxima are observed are different for each microchannel. As a consequence, the wave propagation of X-rays outside a hollow waveguide and the radiation intensity at different positions of the detector can be found only by summing the complex amplitudes of the radiation [see equation (4)]. The calculations we performed show that the smallest spot at the output of the MCP occurs at a distance less than *R*/2.

In Figs. 7(*c*)–7(*d*) the results of our theoretical model of the spot size for radiation focused along the *z*-axis at different distances between the MCP and the detector are compared. Considering the FWHM of the beam profile versus distance the smallest spot and the maximum intensity for the curvature radius of 30 mm at the incident energies of 450 eV, 1000 eV, 1500 eV correspond to *z* = 11.5 mm, *z* = 12 mm and *z* = 12 mm, respectively. All distances are smaller than *R*/2 = 15 mm. As shown in Fig. 7(*d*) the simulations also predict that at the lowest energy (450 eV) the profile is sharper compared with profiles at 1000 eV and 1500 eV. On the other hand, the focus is nearer at high energy compared with that at 450 eV.

Considering a parallel beam, simulations changing the MCP–detector distance are compared in Fig. 8. At 450 eV [Fig. 8(*a*)] the maximum intensity occurs at *z* = 19 mm for the spherically bent MCP with *R* = 50 mm. This value has been taken as the reference for the intensity. At this energy other MCPs transmit less radiation, *e.g.* for *R* = 30 mm, the maximum occurs at *z* = 11.5 mm (~89% of the reference intensity) while, for *R* = 100 mm, *z* = 33 mm and the relative intensity corresponds to 76%.

Figures 8(*b*)–8(*d*) compare simulations performed at 1000 eV. At this energy, the most efficient MCP has a radius *R* = 100 mm. Summarizing, simulations confirm that bent MCPs focus X-rays of different energies at distances correlated to the curvature radius. Figs. 8(*a*) and 8(*b*) point out that
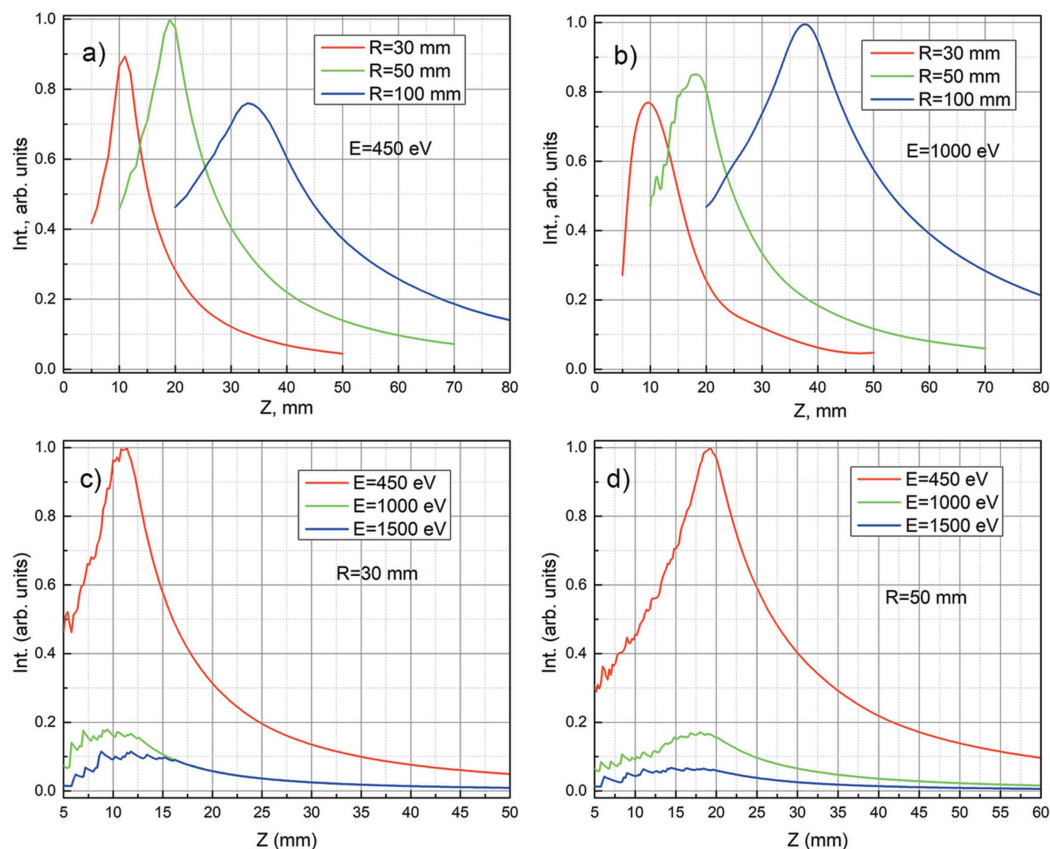
Figure 8
Calculations showing the intensity versus the detector distance (z-axis) among three different spherically bent MCPs at 450 eV [panel (a)]; 1000 eV [panel (b)] and for R = 30 mm [panel (c)] and R = 50 mm [panel (d)] for different energies.

spherical MCPs with large radii are more effective at high energy. As an example, at 450 eV the spherically bent MCP with radius R = 50 mm is more efficient, while at 1000 eV it corresponds to R = 100 mm. Actually, as the energy increases, the critical reflection angle decreases, and for a small curvature (*i.e.* a large radius) a parallel beam should be more efficiently transmitted by microchannels of any spherically bent MCP. However, theoretical modeling and comparison of normalized intensities in Figs. 8(c) and 8(d) show the decrease in the intensity of the transmitted radiation at high energy. This effect can be explained by the reduced 'aperture' of MCPs at high energy, which affects the amount of the primary radiation illuminating the MCP and collected by each deformed microchannel (Dabagov, 2003a). Nevertheless, for each radius of curvature, an optimal focus can be determined along the z-axis at distances less than R/2.

4. Conclusion

MCPs behave as efficient radiation waveguides in transmission. However, these diffractive optics may increase the flux density and focus X-ray radiation offering interesting perspectives for X-ray applications with high brilliant and highly coherent SR sources. In this study, we demonstrated the focusing properties of spherically bent MCPs with different curvature radius using two different synchrotron radiation sources (BESSY and Elettra) over a wide range of energy

from 450 to 1500 eV. To describe the obtained experimental results, not compatible with simple geometrical optical considerations, we applied a model based on the wave propagation of multiply scattered wavefronts. The simulation results of the MCP focusing are in excellent agreement in the energy range 450–1500 eV.

We also measured the X-ray radiation distribution at the exit of spherically bent MCPs along the optical axis. These maps show that the focal distance between the detector and bent MCPs depends on the curvature radius R, and it is always smaller than the geometrical optical value of R/2.

The result is supported by simulations and by experimental data collected with spherically bent MCPs at energies of 1000 eV and 1500 eV, *i.e.* when a small spot is achieved in correspondence to the highest transmitted intensity.

Our experimental apparatus and the theoretical approach we introduced can be successfully applied to measure and to characterize transmission and focusing properties of different spherically bent MCP devices having different radii of curvature for possible applications with synchrotron radiation and other X-ray sources. It is possible to confirm the efficient use of curved MCPs at small dimensions of the coherent soft X-ray profile. Thus, at this stage, the practical use of these devices for focusing can be limited by a shape change for a coherent synchrotron beam.

Working with a coherent plane wave emitted by a third-generation synchrotron radiation source illuminating a sphe-

rical MCP, we can expect the focus dimension to be limited by a few micrometres. However, since MCPs are easy to fabricate at low cost they can be successfully used in many applications where an extremely stable X-ray focus in the micrometre range is required.

References

Bilderback, D. H., Hoffman, S. A. & Thiel, D. J. (1994). *Science*, **263**, 201–203.

Brunton, A. N., Martin, A. P., Fraser, G. W. & Feller, W. B. A. (1999). *Nucl. Instrum. Methods Phys. Res. A*, **431**, 356–365.

Bukreeva, I., Pelliccia, D., Cedola, A., Scarinci, F., Ilie, M., Giannini, C., De Caro, L. & Lagomarsino, S. (2010). *J. Synchrotron Rad.* **17**, 61–68.

Cao, Z., Jin, F., Dong, J., Yang, Z., Zhan, X., Yuan, Z., Zhang, H., Jiang, S. & Ding, Y. (2013). *Opt. Lett.* **38**, 1509.

Chapman, H. N., Nugent, K. A. & Wilkins, S. W. (1993). *Appl. Opt.* **32**, 6316–6332.

Chapman, H. N., Nugent, K. A., Wilkins, S. W. & Davis, T. J. (1990). *J. X-ray Sci. Tech.* **2**, 117–126.

Dabagov, S. B. (2003a). *Phys.-Usp.* **46**, 1053–1075.

Dabagov, S. B. (2003b). *X-ray Spectrom.* **32**, 179–185.

Dabagov, S. B. & Gladkikh, Yu. P. (2019). *Radiat. Phys. Chem.* **154**, 3–16.

Dabagov, S. B., Kumakhov, M. A. & Nikitina, S. V. (1995a). *Phys. Lett. A*, **203**, 279–282.

Dabagov, S. B., Kumakhov, M. A., Nikitina, S. V., Murashova, V. A., Fedorchuk, R. V. & Yakimenko, M. N. (1995b). *J. Synchrotron Rad.* **2**, 132–135.

D'Elia, A., Rezvani, S. J., Cossaro, A., Stredansky, M., Grazioli, C., Li, B. W., Zou, C. W., Coreno, M. & Marcelli, A. (2020). *J. Supercond. Nov. Magn.* **33**, 2383–2388.

Gao, N. & Janssens, K. (2004). *X-ray Spectrometry: Recent Technological Advances*, edited by K. Tsuji, J. Injuk and R. Van Grieken, pp. 89–110. Chichester: John Wiley & Sons.

Gys, T. (2015). *Nucl. Instrum. Methods Phys. Res. A*, **787**, 254–260.

Henke, B. L. Gullikson, E. M. & Davis, J. C. (1993). *At. Data Nucl. Data Tables*, **54**, 181–342.

Kaaret, P., Geissbühler, P., Chen, A. & Glavinas, E. (1992). *Appl. Opt.* **31**, 7339–7343.

Kumakhov, M. A. (2000). *Proc. SPIE*, **4155**, 1–152.

Kumakhov, M. A. & Komarov, F. F. (1990). *Phys. Rep.* **191**, 289–350.

MacDonald, C. A. (2010). *X-ray Opt. Instrum.* **10**, 867049.

MacDonald, C. A. & Gibson, W. M. (2000). *Handbook of Optics*, Volume III, edited by M. Bass, ch. 30, pp. 30.1–30.12. McGraw-Hill.

Marcelli, A., Cibin, G. & Raco, A. (2004). Report LNF-04/6(IR). Laboratori Nazionali di Frascati, Frascati, Italy.

Marcelli, A., Mazuritskiy, M. I., Dabagov, S. B., Hampai, D., Lerer, A. M., Izotova, E. A., D'Elia, A., Turchini, S., Zema, N., Zuccaro, F., de Simone, M., Rezvani, S. J. & Coreno, M. (2018). *J. Instrum.* **13**, C03035.

Mazuritskiy, M. I. (2012). *J. Synchrotron Rad.* **19**, 129–131.

Mazuritskiy, M. I., Dabagov, S. B., Marcelli, A., Lerer, A., Novakovich, A. & Dziedzic Kocurek, K. (2014). *J. Opt. Soc. Am. B*, **31**, 2182–2187.

Mazuritskiy, M. I., Dabagov, S. B., Marcelli, A., Lerer, A. M. & Dziedzic-Kocurek, K. (2016a). *J. Synchrotron Rad.* **23**, 274–280.

Mazuritskiy, M. I., Lerer, A. M., Dabagov, S. B., Marcelli, A., Hampai, D. & Dziedzic Kocurek, K. (2019). *J. Surface Investig.* **13**, 1005–1013.

Mazuritskiy, M. I., Lerer, A. M. & Makhno, P. V. (2016b). *JETP*, **128**, 1084–1093.

Mazuritskiy, M. I., Lerer, A. M., Marcelli, A., Dabagov, S. B., Coreno, M. & D'Elia, A. (2018). *JETP Lett.* **107**, 600–605.

Nussey, P. (2005). PhD Thesis, University of Leicester, UK.

Pasqualini, M., Calcaterra, S., Maroni, F., Rezvani, S. J., Di Cicco, A., Alexander, S., Rajantie, H., Tossici, R. & Nobili, F. (2017). *Electrochim. Acta*, **258**, 175–181.

Pfeiffer, F., David, C., Burghammer, M., Riekel, C. & Salditt, T. (2002). *Science*, **297**, 230–234.

Pinto, N., Rezvani, S. J., Favre, L., Berbezier, I., Fretto, M. & Boarino, L. (2016). *Appl. Phys. Lett.* **109**, 123101.

Rezvani, S. J., Gunnella, R., Neilson, D., Boarino, L., Croin, L., Aprile, G., Fretto, M., Rizzi, P., Antonioli, D. & Pinto, N. (2016). *Nanotechnology*, **27**, 345301.

Rezvani, S. J., Pasqualini, M., Witkowska, A., Gunnella, R., Birrozzi, A., Minicucci, M., Rajantie, H., Copley, M., Nobili, F. & Di Cicco, A. (2018). *Appl. Surf. Sci.* **435**, 1029–1036.

Sanchez del Rio, M. & Marcelli, M. (1992). *Nucl. Instrum. Methods Phys. Res. A*, **319**, 170–177.

Sokolov, A. A., Eggenstein, F., Erko, A., Follath, R., Künstner, S., Mast, M., Schmidt, J. S., Senf, F., Siewert, F., Zeschke, Th. & Schäfers, F. (2014). *Proc. SPIE*, **9206**, 92060J.

Sokolov, A., Sertsu, M. G., Gaupp, A., Lüttecke, M. & Schäfers, F. (2018). *J. Synchrotron Rad.* **25**, 100–107.

Sun, T., Zhang, M., Liu, Z., Zhang, Z., Li, G., Ma, Y., Du, X., Jia, Q., Chen, Y., Yuan, Q., Huang, W., Zhu, P. & Ding, X. (2009). *J. Synchrotron Rad.* **16**, 116–118.

Tsuji, K., Injuk, J. & Van Grieken, R. (2004). Editors. *X-ray Spectrometry: Recent Technological Advances*, p. 616. Chichester: John Wiley & Sons.

Zhang, Q., Zhao, K., Li, J., Chini, M., Cheng, Y., Wu, Y., Cunningham, E. & Chang, Z. (2014). *Opt. Lett.* **39**, 3670–3673.

Zhurong, C., Fengtao, J., Jianjun, D., Zhenghua, Y., Xiayu, Z., Zheng, Y., Haiying, Z., Shaoen, J. & Yongkun, D. (2013). *Opt. Lett.* **38**, 1509–1511.